



Spectral analysis of coherent and incoherent phonon transport in silicon nanomeshes

Haoran Cui , Theodore Maranets, Tengfei Ma, and Yan Wang ^{*}

Department of Mechanical Engineering, University of Nevada, Reno, Reno, Nevada 89557, USA



(Received 7 March 2024; revised 17 July 2024; accepted 19 July 2024; published 2 August 2024)

In this paper, we investigate the spectral thermal transport properties of silicon nanomeshes (SNMs) with large and small holes arranged periodically, aperiodically in the x direction (**ap-x**), and fully aperiodically (**ap-xy**). Our simulations reveal a significant reduction in thermal conductivity (κ) of small-hole SNMs due to **ap-x** aperiodicity, in contrast with large-hole SNMs. Spectral phonon analysis indicates that low-frequency phonons in small-hole SNMs are notably suppressed by **ap-x** aperiodicity, like one-dimensional superlattices. Spectral energy density analysis shows the existence of well-defined coherent phonon modes in small-hole SNMs in the 0–3 THz range; spectral thermal conductivity analysis shows that these modes transport ballistically in the SNM. In contrast, **ap-x** aperiodicity has negligible impact on large-hole SNMs, attributed to hindered coherent phonon formation. Surprisingly, low-frequency phonons in small-hole SNMs demonstrate enhanced heat transfer capabilities compared with large-hole counterparts, highlighting coherent phonon behavior. Finally, while the heat flux splitting and shape factors effectively categorize κ for large-hole SNMs, their utility is limited for small-hole SNMs, emphasizing the importance of coherent phonon considerations in thermal transport analysis.

DOI: [10.1103/PhysRevB.110.075301](https://doi.org/10.1103/PhysRevB.110.075301)

I. INTRODUCTION

Nowadays, the rapid evolution of miniaturized electronic and optoelectronic devices has heightened the demand for effective thermal management strategies. Furthermore, advancements in thermoelectric materials, thermal insulating materials, and other materials for thermal applications necessitate a deliberate design approach toward the thermal transport properties of micro-/nano-sized structures. Understanding the underlying physics of heat transfer in these materials is crucial. Notably, many modern devices or materials exhibit secondary periodicity or quasiperiodicity. For instance, superlattice (SL) structures utilized in quantum cascade lasers exhibit pronounced periodicity in their lattice structure. Similarly, in very large-scale integrated circuits, components are arranged in a manner that demonstrates certain local and long-range periodicity, often at length scales comparable with the mean-free path of heat carriers.

In the last decade, there has been growing acknowledgment of two distinct phonon transport characteristics within materials, particularly those exhibiting secondary periodicity: coherent phonons, displaying significant wavelike behaviors, and incoherent phonons, behaving akin to particles [1–8]. To comprehend these phenomena, researchers have investigated two primary types of nanostructures. The first type includes SLs comprising alternating layers of different materials, organized in a one-dimensional (1D) arrangement [1,3,4,9,10]. The second type comprises nanomeshes (NMs) characterized by micro-/nano-sized through-holes distributed across a two-dimensional (2D) plane [11–16].

While both SLs and NMs have been subjects of investigation regarding potential coherent phonon transport behaviors,

it is important to note their substantial differences in this context. Specifically, in SLs, the interfaces—acting as the primary scatterers of phonons—span the entire cross-section of phonon transport. As a result, SLs provide a clean and clear-cut system for illustrating the transmission, reflection, and interference of phonons [17–19]. In contrast, NMs feature holes distributed on a 2D plane, leaving spaces of solid material between holes and even continuous channels that allow nearly free phonon transport, akin to a pure material or nanowire. Consequently, phonons in NMs do not necessarily encounter scattering from the holes, as illustrated in Figs. 1(a)–1(c). It is evident that SLs offer a more straightforward system for showcasing phonon coherence. Nevertheless, NMs present a more intricate challenge, allowing for a detailed exploration of phonon transport, scattering, and even localization—factors that play a crucial role in various applications, such as energy storage and conversion [20,21].

Coherent phonons, stemming from phonon wave effects, significantly influence lattice thermal conductivity (κ) by altering phonon band gaps, group velocities, and other parameters [1,22,23]. Extensive prior research has elucidated these effects, underscoring their pivotal role in thermal transport phenomena. Notably, Yu *et al.* [11] found a nearly one-order-of-magnitude lower κ of silicon NMs (SNMs) than silicon thin films of the same size, attributing the ultralow κ of the former to the formation of additional coherent phonons through Brillouin zone folding, which significantly reduces phonon group velocities, like the case of 1D SLs [1]. Hopkins *et al.* [24] found that the ultralow values of κ of SNMs substantially deviate from theoretical predictions based solely on hole-boundary phonon scatterings. Investigations into the phonon density of states revealed significant disparities from those of bulk silicon, providing evidence for the emergence of additional phonon dispersion relations attributed to coherent phonon formation. Furthermore, the

^{*}Contact author: yanwang@unr.edu

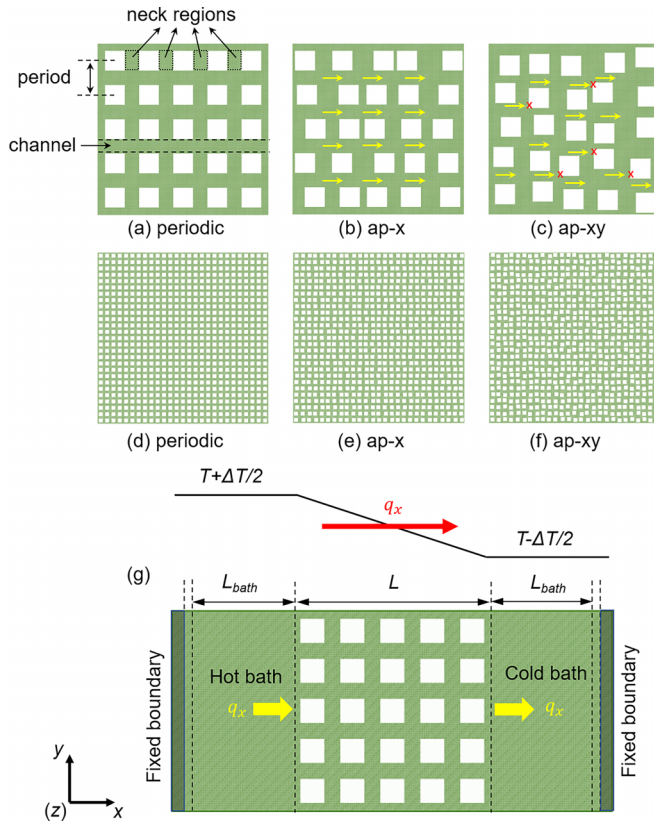


FIG. 1. Schematics of the silicon nanomesh (SNM) structures and the domain setup of nonequilibrium molecular dynamics (NEMD) simulation in LAMMPS. Large-hole SNMs with distinct hole arrangements: (a) A typical periodic SNM featuring periodically arranged holes. (b) A representative **ap-x** SNM with randomly distributed holes exclusively along the x direction. (c) A representative **ap-xy** SNM with randomly distributed holes along both x and y directions. (d)–(f) Three hole arrangements for small-hole SNMs. (g) NEMD domain setup, where L_{bath} (34 nm) denotes the length of the heat bath, and L (65 nm) represents the device length. The hot and cold baths maintain temperatures at $T + \Delta T/2$ and $T - \Delta T/2$, respectively, where $T = 300$ K and $\Delta T = 60$ K. q_x represents the heat flux in the device.

notable experiments by Zen *et al.* [12] on silicon nitride (SiN) NMs at temperatures < 1 K revealed a substantial suppression of phonon transport compared to bulk SiN. This suppression was attributed to coherent modification of the phonon band structure induced by the periodic holes in SiN NMs. Alaie *et al.* [13] provided additional experimental evidence of coherent phonon boundary scattering at room temperature in submicron-sized SNMs, demonstrating its significant impact on reducing κ . Wagner *et al.* [14] conducted experiments on SNMs with varying surface roughness and aperiodic hole distributions. Their findings revealed that aperiodicity in hole locations can modify phonon dispersion relations and coherence in the hypersonic (GHz) range without significantly impacting room-temperature κ . Additionally, they observed that phonon coherence remains intact when surface roughness is $< \frac{1}{25}$ of the phonon wavelength but is disrupted beyond $\frac{1}{10}$ of the phonon wavelength.

Through the aforementioned studies and others not explicitly discussed, it becomes evident that coherent phonons

can significantly influence the thermal transport properties of NMs. However, this influence is subject to various structural and thermodynamic considerations [25,26]. Consequently, the manifestation of phonon coherence in patterned films or NMs is not assured. While coherent phonon behaviors are observed in some cases, more frequently, phonons exhibit incoherent behaviors, resembling particles rather than coherent waves. For instance, in a comparative study by Lee *et al.* [15] between periodic and aperiodic SNMs, no significant difference in κ was observed between the two structures, suggesting the limited importance of phonon coherence in this context. In the study by Maire *et al.* [27] on the temperature-dependent behavior of SNMs with varied degrees of disorder in hole locations, it was observed that, while periodic SNMs showed suppressed thermal transport compared with aperiodic ones at 4 K, attributed to coherent phonon scattering, this difference diminished at higher temperatures and vanished completely at 300 K. This trend suggests that phonon interference predominantly occurs in ordered phononic crystals only at low temperatures.

Theoretical and computational methods have provided insights into phonon thermal transport in NMs. Molecular dynamics (MD) simulations have highlighted the dependence of κ on hole shapes, and phonon scattering and localization have been identified as influencing factors [26,28,29]. Additionally, MD simulations of graphene NMs (GNMs) with periodic and aperiodic holes have shown a transition from incoherent to coherent thermal transport as the period length decreases [30]. However, it is notable that, while most MD studies found the κ of aperiodic NMs to be less than or similar to that of their periodic counterparts, this contradicts some experimental findings indicating that the periodic structure minimizes κ due to coherent phonon backscattering [15]. In a recent study using Boltzmann transport simulations, a genetic algorithm-driven approach identified GNM structures with higher κ than their periodic counterparts. However, the increased κ appears to result from enhanced transport of incoherent phonons rather than enhanced coherent phonon transport [31]. Moreover, a comparison between MD and Boltzmann transport equation (BTE) results by Wei *et al.* [32] showed that the coexistence of coherent and incoherent phonon behaviors in periodic and aperiodic GNMs collectively determines their κ . This phenomenon resembles the behavior observed in 1D SLs, where the coexistence of coherent and incoherent phonons leads to ballistic thermal transport in SLs and more complex thermal transport behaviors in aperiodic structures [3,4,33–36].

Despite extensive experimental, theoretical, and computational investigations into phonon behaviors in NMs, several crucial aspects remain unclear. In this paper, we aim to tackle the following unresolved questions. First, how do different phonon modes in NMs propagate—coherently or incoherently, ballistically or diffusively? Secondly, how does the aperiodicity in hole locations impact different phonon modes? Which modes are prone to be suppressed by such aperiodicity? Thirdly, what is the influence of hole size on phonon coherence? While some of these questions, such as the second and third ones, have been partially addressed through experiments or modeling studies [30], they have primarily focused on overall thermal transport properties like κ or thermal

decay rate. A comprehensive understanding of phonon behavior on a mode-by-mode basis could significantly enhance the design of phonon engineering strategies to better regulate thermal transport in NMs.

This paper is structured as follows. In Sec. II, we outline the computational methodologies employed, including equilibrium MD (EMD) and nonequilibrium MD (NEMD) for calculating bulk-limit and length-dependent κ of SNMs, and spectral phonon analysis methods; we also introduce the model systems. Section III A details MD results of κ for SNMs with different aperiodicities and hole sizes. Section III B elucidates the effect of holes on spectral phonon transport. Sections III C and III D discuss the effect of device length on spectral phonon transport in large- and small-hole SNMs, respectively. Sections III E and III F investigate the effectiveness of heat flux splitting and shape factor in categorizing SNM κ . Finally, we conclude this paper in Sec. IV.

II. METHODOLOGY

A. EMD

We perform EMD simulations using the LAMMPS package [37] with the interatomic interactions between silicon atoms described by the Stillinger-Weber potential [38]. The SNM structure simulated in our EMD simulations for κ has 110, 110, and 2 conventional unit cells of silicon in the length (x), width (y), and thickness (z) directions, corresponding to $59.7 \times 59.7 \times 1.1$ nm. A simulation time step size of 0.5 fs is utilized, and periodic boundary conditions are imposed in all three dimensions. In the initial relaxation process, the system temperature is gradually elevated from 5 to 300 K over a duration of 1 ns using a Nosé-Hoover thermostat and barostat in the NPT ensemble. Subsequently, an additional 2 ns of constant NPT integration is conducted to ensure the system is relaxed at 300 K. The heat fluxes are then recorded for 7.5 ns within the microcanonical (NVE) ensemble. These fluxes are then utilized in Green-Kubo calculations to evaluate the κ of SNM along the heat flow direction. Specifically, κ along the x direction can be calculated as [39]

$$\kappa_x = \frac{V}{k_B T^2} \int_0^\infty \langle J_x(t) J_x(0) \rangle dt, \quad (1)$$

where k_B is the Boltzmann constant, T is the ambient temperature, V is the system volume, t is the time, and J_x is the heat flux in the x direction. Here, $\langle J_x(t) J_x(0) \rangle$ is the heat flux autocorrelation function.

B. Model systems

Figure 1(a) depicts the periodic large-hole SNM studied in this paper, where each through-hole is $\sim 7.2 \times 7.2$ nm. Accordingly, the unit cell of the periodic large-hole SNM is 12×12 nm, containing one hole, corresponding to a period length of 12 nm in both the x and y directions, as denoted in Fig. 1(a). Figure 1(d) displays the periodic small-hole SNM studied in this paper, with each hole measuring $\sim 1.5 \times 1.5$ nm. The unit cell of the periodic small-hole SNM, containing a small hole, is 2.2×2.2 nm, much smaller than that of the large-hole counterparts. Notably, when generating small-hole

SNMs, we ensured that both large- and small-hole SNMs have the same porosity.

Figures 1(b) and 1(e) exhibit representative **ap-x** SNM structures investigated in this paper, generated by shifting holes in the corresponding periodic SNM by a random distance only along the x direction. Similarly, the **ap-xy** SNMs in Figs. 1(c) and 1(f) are obtained by displacing the holes in the corresponding periodic SNM by random distances along both the x and y directions. Notably, the displacements of holes in the x and/or y directions are randomly generated, following a uniform distribution between $[-4\text{UC}, +4\text{UC}]$ for large-hole SNMs and $[-1\text{UC}, +1\text{UC}]$ for small-hole SNMs, where UC denotes the size of the unit cell of silicon (5.43 Å). The statistical distribution of hole displacements is shown in Fig. S9 in the Supplemental Material [40].

While it is not within the scope of this paper to investigate how phonon properties vary with the extent of aperiodicity in the **ap-x** and **ap-xy** SNM structures, it is important to recognize its crucial impact. Multiple numerical studies, often combined with machine-learning techniques, have explored how aperiodicity affects the thermal conductivity of SNMs, GNMs, and SLs [36,41], with the aim of minimizing κ . The general conclusion is that κ can approach the minimized value by simply randomizing the hole locations in NM structures or the layer thicknesses in SLs. In this paper, we generate the **ap-x** and **ap-xy** SNM structures by randomizing the hole locations to the full extent (i.e., two holes can nearly meet each other).

To further confirm that the hole locations of our **ap-x** and **ap-xy** structures are well randomized, we generate two additional **ap-x** and **ap-xy** structures with different hole locations. As shown in Table R1 in the Supplemental Material [40], the κ 's, predicted from EMD, of the three samples in each case are similar, all significantly lower than the κ 's of their periodic counterparts. This confirms the sufficient disorder in hole locations of our **ap-x** and **ap-xy** structures.

C. NEMD

The NEMD simulations in this paper adopt the same time step size and boundary conditions as those in the EMD simulations. The SNM structure simulated in our NEMD simulations has 250, 110, and 2 conventional unit cells of silicon in the length (x), width (y), and thickness (z) directions, corresponding to $135.8 \times 59.7 \times 1.1$ nm.

In NEMD, following the identical structural relaxation process as described in Sec. II A, two 0.7-nm-thick layers [as indicated in Fig. 1(g)] at the two ends of the model are frozen as fixed boundaries. Subsequently, the simulation is switched to plain time integration defined in LAMMPS for 7.5 ns to establish steady-state heat transfer, during which the hot and cold baths (34 nm long for each bath) are maintained at $T + \Delta T/2$ and $T - \Delta T/2$, respectively. In this paper, T is set as 300 K, and ΔT is 60 K.

The value of κ is deduced from the steady-state heat current and temperature gradient based on Fourier's law:

$$\kappa = \frac{q_x L}{\Delta T A_c}, \quad (2)$$

where $A_c = 59.7 \times 1.1$ nm is the cross-sectional area of the device, which is independent of the porosity of the SNM. In addition, q_x is the steady-state heat current, L is the length of the device, and ΔT is the temperature bias between hot and cold baths.

D. Heat flux vector calculation

The per-atom heat flux vector, which provides insight into location-dependent thermal transport inside the structure, can be evaluated as

$$J = \frac{1}{V} \left[\sum_i e_i v_i - \sum_i S_i v_i \right], \quad (3)$$

in which i is the atomic index, e_i is the per-atom energy (potential and kinetic), v_i is the atom velocity in a specific direction, and S_i is the per-atom stress tensor.

E. Spectral thermal conductivity

To investigate the predominant mechanisms influencing phonon transport in various SNM structures, we perform spectral phonon thermal conductivity analysis through NEMD simulations. Specifically, the spectrally decomposed heat flux in our NEMD simulations is calculated with Eq. (4) to quantify spectral phonon heat flux [42,43]:

$$Q(\omega) = \sum_{i \in \tilde{L}} \sum_{j \in \tilde{R}} \left[-\frac{2}{t_{\text{simu}} \omega} \sum_{\alpha, \beta} \text{Im} \langle \hat{v}_i^\alpha(\omega)^* K_{ij}^{\alpha\beta} \hat{v}_j^\beta(\omega) \rangle \right], \quad (4)$$

in which $Q(\omega)$ is spectral heat flux; ω is frequency; i and j are, respectively, the atom indices in the left (\tilde{L}) and right (\tilde{R}) part of the cross-section locating in the middle of the device; t_{simu} is the total NEMD simulation time; α and β are Cartesian coordinates with values of x , y , and z ; \hat{v} is the Fourier transform of atom velocity; $*$ denotes the complex conjugate operator; and $K_{ij}^{\alpha\beta}$ is the force constant matrix.

Specifically, according to Eq. (4), we decompose the spectra into contributions by each polarization in x , y , and z directions as

$$Q_x(\omega) = \sum_{i \in \tilde{L}} \sum_{j \in \tilde{R}} \left[-\frac{2}{t_{\text{simu}} \omega} \sum_{\beta=x,y,z} \text{Im} \langle \hat{v}_i^x(\omega)^* K_{ij}^{x\beta} \hat{v}_j^\beta(\omega) \rangle \right], \quad (5)$$

$$Q_y(\omega) = \sum_{i \in \tilde{L}} \sum_{j \in \tilde{R}} \left[-\frac{2}{t_{\text{simu}} \omega} \sum_{\beta=x,y,z} \text{Im} \langle \hat{v}_i^y(\omega)^* K_{ij}^{y\beta} \hat{v}_j^\beta(\omega) \rangle \right], \quad (6)$$

$$Q_z(\omega) = \sum_{i \in \tilde{L}} \sum_{j \in \tilde{R}} \left[-\frac{2}{t_{\text{simu}} \omega} \sum_{\beta=x,y,z} \text{Im} \langle \hat{v}_i^z(\omega)^* K_{ij}^{z\beta} \hat{v}_j^\beta(\omega) \rangle \right]. \quad (7)$$

To ensure fair comparisons among SNMs of varying lengths, spectral thermal conductivity $\kappa(\omega)$ arises as an optimal parameter. It is calculated as

$$\kappa(\omega) = \frac{\kappa}{\int_0^\infty Q(\omega) d\omega} Q(\omega). \quad (8)$$

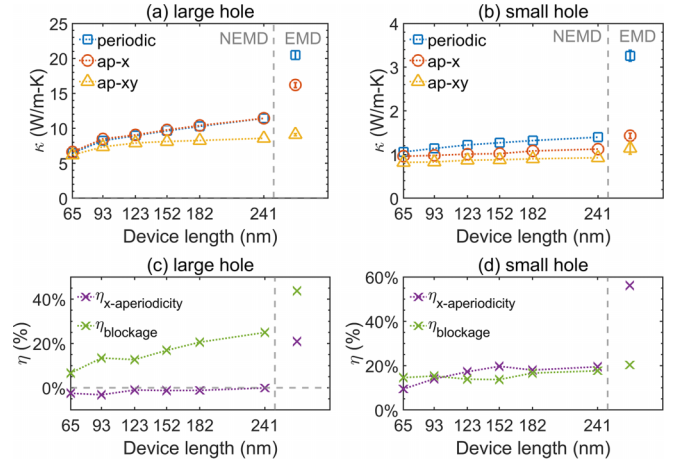


FIG. 2. Length-dependent κ of silicon nanomeshes (SNMs) at 300 K. (a) κ values obtained from both nonequilibrium molecular dynamics (NEMD) and equilibrium molecular dynamics (EMD) for large-hole SNMs. (b) κ values derived from both NEMD and EMD for small-hole SNMs. (c) and (d) Parameter η , as defined in Eqs. (11a) and (11b), for large- and small-hole SNMs, respectively.

F. Spectral energy density analysis

Phonon spectral energy density (SED) quantifies the kinetic energy of a phonon mode. It is defined on the time-domain normal mode coordinates $q_{k,v}(t)$ as [44,45]

$$q_{k,v}(t) = \sum_{\alpha}^3 \sum_b^n \sum_l^{N_c} \sqrt{\frac{m_b}{N_c}} u_{\alpha}^{l,b}(t) e_{b,\alpha}^{k,v*} \exp[i\mathbf{k} \cdot \mathbf{r}_0^l], \quad (9)$$

where $u_{\alpha}^{l,b}(t)$ represents the α th component of the displacement of the b th-basis atom in the l th unit cell, m_b is atomic mass, N_c is the total number of primitive unit cells of the entire system, t is time, \mathbf{k} denotes the wave vector, v is phonon polarization, and \mathbf{r}_0 is the equilibrium position of each unit cell. Here, $q_{k,v}(t)$ data are collected from EMD in the NVE ensemble for 250 ps, ensuring a high resolution of 0.004 THz for analyzing phonon properties in the frequency domain. Subsequently, SED is calculated through Fourier transform ($\mathcal{F}[\cdot]$) of the time derivative of $q_{k,v}(t)$ as

$$\Phi_{\mathbf{k},v}(\omega) = |\mathcal{F}[\dot{q}_{k,v}(t)]|^2 = \frac{C_{\mathbf{k},v}}{(\omega - \omega_{\mathbf{k},v}^A)^2 + (\tau_{\mathbf{k},v}^{-1})^2/4}, \quad (10)$$

where $\Phi_{\mathbf{k},v}(\omega)$ is the SED, ω is the angular frequency, and C is a constant. The transformed data can be fitted with the Lorentzian function to obtain the peak position $\omega_{\mathbf{k},v}^A$ and phonon lifetime ($\tau_{\mathbf{k},v}$).

III. RESULTS AND DISCUSSIONS

A. The effect of hole size and periodicity on κ : EMD and NEMD results

Figure 2 illustrates the NEMD and EMD results for κ as a function of the device length L of both large-hole (7.2×7.2 nm²) and small-hole (1.5×1.5 nm²) SNM configurations, featuring periodic and aperiodic hole distributions. The NEMD results demonstrate the length-dependent

behavior of SNMs, while the EMD data correspond to the bulk limit κ for each SNM structure [46].

In Fig. 2, we present results for two aperiodic structures: the **ap-x** SNM, where holes exhibit aperiodicity solely in the x (heat flow) direction, and the fully aperiodic SNM, denoted as the **ap-xy** SNM. We chose to investigate the **ap-x** structure to isolate the impact of aperiodicity in hole locations along the heat flow direction on phonon transport. This configuration mirrors the scenario of 1D aperiodic SLs, which exhibit aperiodicity only in the interface locations along the heat flow direction, known to suppress coherent phonon transport [4,47,48]. In contrast, the fully aperiodic **ap-xy** SNM structure can reduce κ through both y -direction (perpendicular to heat flow) aperiodicity, which obstructs phonon transport in the otherwise straight channels, and x -direction aperiodicity, thereby complicating the mechanism underlying the reduction in κ .

As displayed in Fig. 2(a), the κ values of both periodic and **ap-x** large-hole SNMs increase with device length. Notably, the κ of the 241-nm-long large-hole SNM is $\sim 43\%$ lower than its bulk limit κ for the periodic structure, and it is $\sim 29\%$ for the **ap-x** structure. This suggests prominent ballistic thermal transport characteristics. In contrast, **ap-xy** large-hole SNMs exhibit almost constant κ when the device length surpasses 123 nm, with the κ of the 241-nm-long structure only $\sim 6\%$ lower than its bulk limit value, indicating diffusive thermal transport and substantial phonon scattering.

Results for small-hole SNM in Fig. 2(b) exhibit distinctive features compared with large-hole SNM data in Fig. 2(a). First, the κ values for small-hole SNMs are notably lower than those for their large-hole counterparts. Second, the κ of the 241-nm-long periodic small-hole SNM is lower than its bulk limit value by as much as 57%, while it is only 43% for the large-hole case [Fig. 2(a)], indicating stronger ballistic phonon transport in the small-hole case. Third, unlike large-hole SNMs, for which $\kappa_{\text{periodic}} \approx \kappa_{\text{ap-x}}$, the κ of small-hole SNMs is significantly reduced by hole aperiodicity in the x direction.

To quantify the effect of x -direction aperiodicity and blockage (the additional y aperiodicity) on κ , we define η as

$$\eta_{x\text{-aperiodicity}} = 1 - \frac{\kappa_{\text{ap-x}}}{\kappa_{\text{periodic}}}, \quad (11a)$$

$$\eta_{\text{blockage}} = 1 - \frac{\kappa_{\text{ap-xy}}}{\kappa_{\text{ap-x}}}. \quad (11b)$$

Here, $\eta_{x\text{-aperiodicity}}$, comparing κ_{periodic} and $\kappa_{\text{ap-x}}$, quantifies the impact of aperiodicity in the x (heat flow) direction on κ , while η_{blockage} , comparing $\kappa_{\text{ap-x}}$ and $\kappa_{\text{ap-xy}}$, assesses the effect of aperiodicity in the y direction in further reducing κ . As illustrated in Fig. 2(c), the influence of x aperiodicity on κ in large-hole SNMs is negligible, and the reduced κ of **ap-xy** SNMs is solely attributed to the aperiodic hole arrangement in the cross-section, impeding phonon transport in otherwise straight channels. In contrast, Fig. 2(d) highlights a significantly more pronounced effect of x -direction aperiodicity comparable with the blockage effect induced by y aperiodicity in small-hole SNMs. In the following sections, we will spectrally analyze the behaviors of various phonon modes as affected by x -direction aperiodicity, y -direction aperiodicity,

and SNM length to elucidate possible coherent and incoherent phonon behaviors.

B. Effect of hole size and periodicity on spectral phonon transport

Figures 3(a) and 3(b) show the thermal conductivity spectra $\kappa(\omega)$ of large-hole SNMs [panel (a)] and small-hole SNMs [panel (b)], and Fig. 3(c) compares the $\kappa(\omega)$ of SNMs with that of pristine silicon without any holes.

In panel (a), the green shaded area ($\kappa_{\text{periodic}} - \kappa_{\text{ap-x}}$) illustrates that the x -direction aperiodicity in hole positions minimally affects phonon transport in large-hole SNMs. In contrast, as illustrated by the red shaded area, the full aperiodicity of the **ap-xy** SNM structure significantly impedes the transport of low- to midfrequency (3.3–6.8 and 10.8–13 THz) phonons. These observations align with the thermal conductivity data in Fig. 2(a), confirming the limited impact of x -direction aperiodicity on phonon transport in large-hole SNMs.

Contrarily, Fig. 3(b) reveals substantial suppression of phonon transport in both **ap-x** and **ap-xy** small-hole SNMs. The green shaded area indicates that x -direction aperiodicity suppresses the transport of low-frequency acoustic phonons due to the disruption of phonon modes in an otherwise periodic structure. We hypothesize that the decrease in $\kappa(\omega)$ and κ of **ap-x** SNMs shares similar physics with the reduced $\kappa(\omega)$ and κ observed in aperiodic SLs [19]. Additionally, the introduction of y -direction aperiodicity, resulting in an **ap-xy** SNM structure, further suppresses the transport of low-frequency phonons, primarily due to the obstruction of transport channels.

In Fig. 3(c), we compare the $\kappa(\omega)$ of pristine silicon, large-hole SNM, and small-hole SNM. Notably, holes, regardless of size, suppress a broad spectrum of phonon thermal transport, as evidenced by the nearly one-order-of-magnitude higher $\kappa(\omega)$ curve of pristine silicon than that of SNMs. Moreover, the extent of suppression varies with frequency, exhibiting a more pronounced reduction (in ratio) of higher-frequency phonons than lower-frequency ones, indicating stronger hole scattering of phonons of higher frequency.

Furthermore, Fig. 3(c) illustrates that the thermal conductivity spectra of small-hole SNMs is significantly lower than that of large-hole SNMs, consistent with the expectation that smaller holes, being more numerous (since the total hole area is fixed in this paper), can scatter phonons more effectively than larger holes. This behavior mirrors nanoparticle scattering of phonons, well understood both experimentally [49] and theoretically [50].

Of particular interest, Fig. 3(c) reveals that the lowest-frequency phonons (0–2.2 THz) in the small-hole SNM exhibit even higher spectral thermal conductivity $\kappa(\omega)$ than phonons of the same frequency in the large-hole SNM counterpart. We attribute this phenomenon to coherent phonon transport behaviors like those observed in SLs. Within small-hole SNMs, the phonon modes of pure silicon can form additional phonon modes corresponding to the altered phonon dispersion inherent to the SNM structure, akin to the emergence of coherent phonons in SLs. Figure 3(d) displays the SED contour (heat map) extracted from our EMD simulations

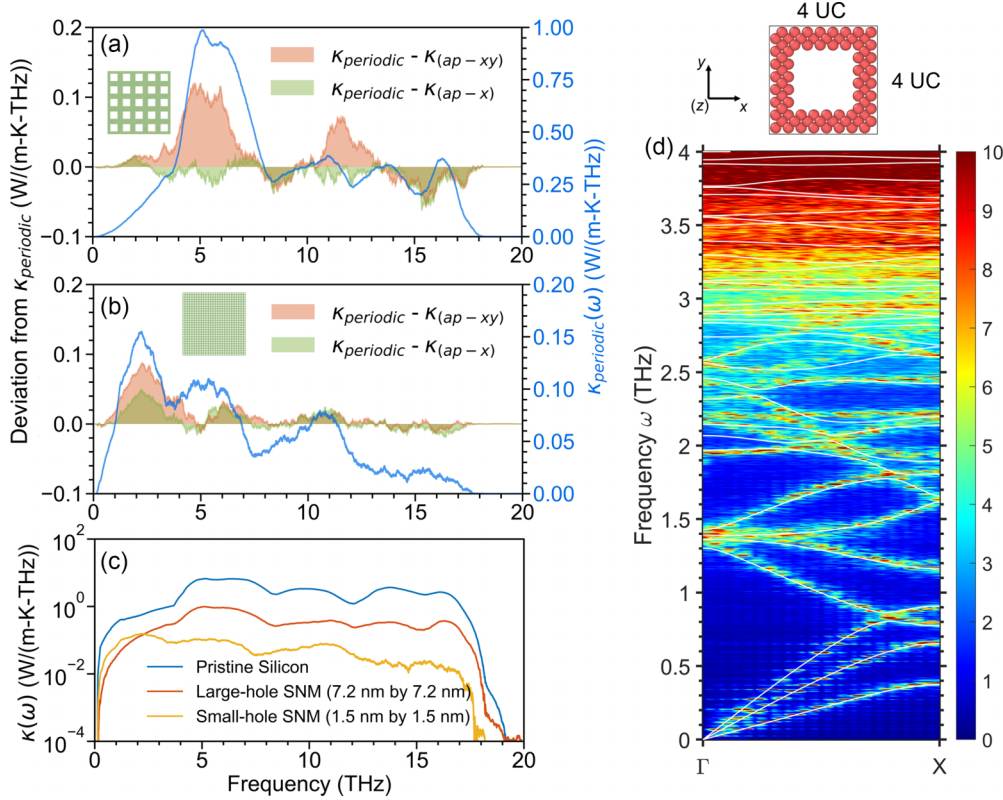


FIG. 3. Illustrations of the thermal conductivity spectra $\kappa(\omega)$ and phonon spectral energy density are shown. (a) Spectrum of large-hole silicon nanomeshes (SNMs). (b) Spectrum of small-hole SNMs. Specifically, the blue curve plotted against the right axis depicts the spectral thermal conductivity $\kappa_{\text{periodic}}(\omega)$ of SNMs with a periodic arrangement of holes. The shaded areas plotted against the left axis represent the deviation from $\kappa_{\text{periodic}}(\omega)$ for SNMs with **ap-x** and **ap-xy** distributions of holes. (c) Spectrum of pristine silicon, large-hole SNM, and small-hole SNM plotted against a logarithmic Y axis. (d) Logarithmic spectral energy density (SED) contour (heat map) at 300 K plotted in the wave vector–frequency domain, along with the phonon dispersion relations from harmonic lattice dynamics (white curves) for the small-hole SNM. Only the 0–4 THz range is plotted in (d), while the full SED contour is displayed in Fig. S1 in the Supplemental Material [40].

of the small-hole SNM, vividly revealing acoustic and a few optical phonon branches that differ from those in the pristine silicon dispersion relations (Supplemental Material [40]). Additionally, we calculate the phonon dispersion relations using the unit cell of the small-hole SNM, which contains a hole; these are displayed as white curves in Fig. 3(d). Evidently, these curves match well with the phonon branches in the SED contour.

Performing SED analysis or lattice dynamics for the large-hole SNM is challenging, if not impossible, due to the excessive computational cost associated with its much larger unit cell (containing thousands of atoms). To evaluate the extent of phonon coherence in both small- and large-hole SNMs, we compute the phonon spatial coherence length of silicon from SED data. As shown in Fig. S1(c) in the Supplemental Material [40], the coherence length in the low-frequency limit is on the order of a few nanometers. This length is larger than the unit cell size of the small-hole SNM (2.2 nm), suggesting significant phonon coherence, and slightly smaller than the unit cell size of the large-hole SNM (12 nm), indicating a certain degree of coherence.

The above SED results [Fig. 3(d)], lattice dynamics results [Fig. 3(d)], and phonon spatial coherence length results (Fig. S1(c) in the Supplemental Material [40]) all demonstrate

the significant coherent phonon nature of the low-frequency phonons in small-hole SNMs and even considerable coherence for the large-hole SNM structure. This understanding helps explain the lower $\kappa(\omega)$ of the large-hole SNM compared with the small-hole SNM in the low-frequency limit through two mechanisms also observed for SLs. First, larger band gaps are formed in the phonon dispersion relations of SNMs with larger holes (or larger unit cells), reducing the average phonon group velocity. Figure S2 in the Supplemental Material [40] clearly demonstrates the increasing band gap with increasing hole size. Second, Baer *et al.* [51] found increased anharmonic phonon scattering phase space in SLs with larger periods, which increases phonon scattering and thus reduces κ . We expect a similar mechanism in SNMs, with increased scattering when the hole size (or unit cell) becomes larger. This is confirmed by the increased phonon scattering rate in larger-hole SNMs found through SED analysis (Fig. S3 in the Supplemental Material [40]). Overall, both mechanisms, arising from the coherent phonon nature of these low-frequency modes, lead to reduced κ of larger-hole SNMs, consistent with our observations in Fig. 3(c).

As a final note of this subsection, it is beneficial to compare our MD results with the previous study by Ravichandran and Minnich [52], who employed the BTE to simulate phonon

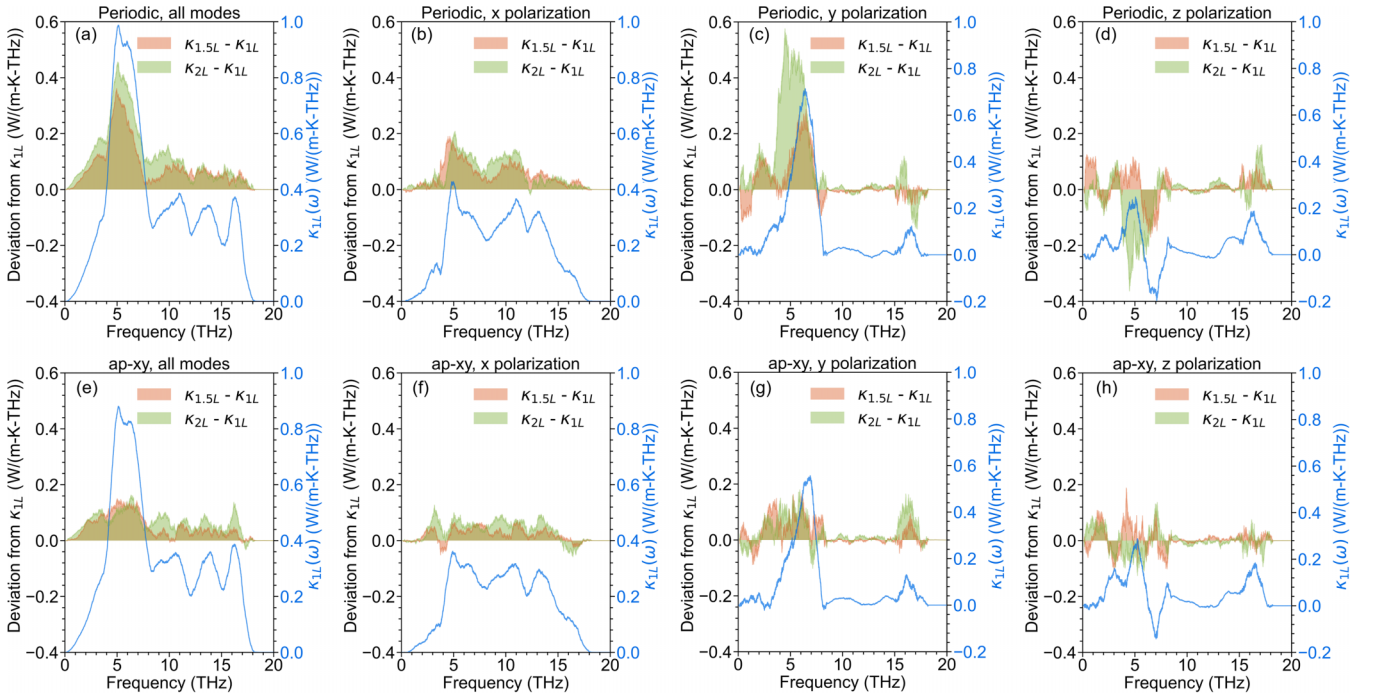


FIG. 4. Left axis (shaded area): Length-dependent deviation from spectral κ of large-hole silicon nanomeshes (SNMs) with length of $1L$ (κ_{1L} , where the subscript L denotes a device length of $L = 65$ nm); right axis (blue curve): spectral κ of κ_{1L} . (a) and (e) Contributions of spectral κ from all modes for periodic and **ap-xy** SNMs, respectively. (b) and (f) Contributions from x polarization. (c) and (g) Contributions from y polarization. (d) and (h) Contributions from z polarization.

thermal transport in SNMs. In their work [52], a larger hole size of 11 nm and a periodicity of 34 nm were used, corresponding to the incoherent phonon regime in this paper. Notably, in Fig. 3(a), we predicted that phonons with a frequency of 5 THz contribute the most to the κ of large-hole SNM. This finding agrees with the BTE predictions of Ravichandran and Minnich [52], where they found a dominant contribution to κ by 5 THz phonons at room temperature. Additionally, their work suggests that a secondary periodicity on the order of 1–2 nm is required to induce significant coherent phonon effects. This is indeed the case in our small-hole SNMs, which have a periodicity (or unit cell size) of 2.2 nm. This agreement further supports our conclusion that the phonons, particularly the low-frequency ones, in the small-hole SNMs studied here exhibit significant coherent nature, while the large-hole SNM demonstrates more incoherent properties. Thus, in the following sections, we will analyze and compare the detailed phonon transport properties of small- and large-hole SNMs to elucidate the distinct behaviors of coherent and incoherent modes in this unique type of metamaterial.

C. Large-hole SNMs: Effect of device length on spectral phonon transport

Figure 4 displays thermal conductivity spectra $\kappa(\omega)$ in the frequency domain for both periodic and **ap-xy** SNMs of varying lengths. In Fig. 4(a), shaded areas represent the deviation of $\kappa(\omega)$ for a $1.5L$ -long (in red) and a $2L$ -long (in green) SNM from that of their $1L$ -long counterpart, where $L = 65$ nm. It is

evident that an increase in device length induces a substantial length-dependent effect on $\kappa(\omega)$. Notably, the contribution of low-frequency phonons to κ increases more significantly as the device length increases, aligning with the characteristic longer mean-free path of these phonons.

In Fig. 4(e), the blue curve represents the $\kappa(\omega)$ of the $1L$ -long **ap-xy** SNM studied in this paper. A direct comparison with the blue curve in Fig. 4(a) reveals an overall lower magnitude, corresponding to the lower κ of the **ap-xy** SNM compared with its periodic counterpart, as presented in Fig. 2(a). Furthermore, $\kappa(\omega)$ displays less significant changes with length compared with the case of periodic SNMs in Fig. 4(a). This observation aligns with the diffusive nature of **ap-xy** SNMs, as manifested in the length-dependent κ data in Fig. 2(a).

In Fig. S5 in the Supplemental Material [40], we present the thermal conductivity spectra $\kappa(\omega)$ of **ap-x** large-hole SNMs, which are nearly the same as the spectra of their periodic counterparts, agreeing with our NEMD results presented in Fig. 2(a), which shows similar values of κ of periodic and **ap-x** large-hole SNMs.

To gain a better understanding of the behavior of each phonon polarization when device length increases, we decompose the spectra in Figs. 4(a) and 4(e) into contributions by each polarization in the x , y , and z directions, corresponding to atomic movements in each direction. Approximately, x -, y -, and z -polarization movements represent the longitudinal modes, in-plane (perpendicular to the axial direction of nanoholes) transverse modes, and cross-plane (parallel to the axial direction of nanoholes) transverse modes.

It is worth noting that this approximation is acceptable only when thermal transport in the x direction is predominantly contributed by phonons with a wave vector in the x direction, i.e., the heat flow direction. If this condition is not met, transverse phonons traveling in oblique directions can have atomic displacements in the x direction; similarly, longitudinal phonons traveling in oblique directions can have atomic displacements in the y and z directions. However, the SNM structures studied in this paper act as phonon direction filters, primarily allowing the transmission of normal-incident phonons while strongly scattering or blocking those traveling in oblique directions, as schematically illustrated in Fig. S8 in the Supplemental Material [40]. Further evidence supporting this point is that the frequency range with prominent values of x -polarized $\kappa(\omega)$, as shown in Fig. 4(b), matches well with the frequency range of the longitudinal acoustic (LA) and longitudinal optical (LO) branches of pristine silicon in Fig. S1 in the Supplemental Material [40]. Similarly, the frequency range with prominent values of y - and z -polarized $\kappa(\omega)$ in Figs. 4(c) and 4(d), respectively, matches well with the frequency range of the transverse acoustic (TA, 0–6.5 THz) and transverse optical (TO, 13–18 THz) branches of silicon shown in Fig. S1 in the Supplemental Material [40].

A comparison of Figs. 4(b)–4(d) shows that the x - and y -polarized phonons contribute most to thermal transport in periodic SNMs, while the z polarization contributes much less and, in certain frequency ranges [notably, 6–8 THz in panel (d) and 6.2–7.7 THz in panel (h)], even contributes negatively. We will discuss the characteristics of $\kappa(\omega)$ for each polarization below.

1. x polarization

As depicted in Fig. 4(b), the thermal conductivity spectra $\kappa(\omega)$ of the large-hole SNM exhibit significant values across a broad frequency range from 0 to 18 THz, corresponding approximately to the dispersive LA and LO branches in Fig. S1(a) in the Supplemental Material [40].

As evidenced by the comparison between Figs. 4(b) and 4(f), aperiodicity in the hole distribution leads to a slight suppression of $\kappa(\omega)$ of LA phonons for the 65-nm-long SNM. As illustrated in Fig. 4(b), $\kappa(\omega)$ exhibits a notable increase with L for periodic SNM, indicating considerable ballistic transport characteristics, which agrees with the κ data in Fig. 2(a). In contrast, the increase is only marginal for the **ap-xy** SNM, indicating primarily diffusive thermal transport, again agreeing with the κ data in Fig. 2(a). Consequently, in longer SNMs (e.g., 2L SNM), there is a pronounced suppression of $\kappa(\omega)$ attributed to the aperiodicity in the hole distribution.

2. y polarization

In comparison with the x -polarization spectra presented in Fig. 4(c), y -polarized modes, predominantly in-plane TA and TO modes, make a more significant contribution to thermal transport in the low-frequency range ($\omega < 8.2$ THz). However, beyond 8.2 THz, the κ of y -polarized phonons diminishes almost to zero. This observation approximately aligns with the fact that the in-plane TA branch terminates at 6.5 THz (as displayed in the phonon dispersion relations in Fig. S1(a) in the Supplemental Material [40]), resulting in a

zero-transmission range corresponding to the band gap in the phonon dispersion relation of silicon.

Despite the narrower $\kappa(\omega)$ spectra of in-plane transverse phonons compared with that of longitudinal ones, their respective total contributions to κ are comparable, as quantified by the total area under the blue $\kappa(\omega)$ curve in Figs. 4(b) and 4(c). In other words, LA, LO, and in-plane TA modes are the major heat carriers in the large-hole SNMs studied in this paper.

The shaded areas in Fig. 4(c) depict the deviation of the $\kappa(\omega)$ of 2L- and 1.5L-long SNMs from their L -long counterpart. Evidently, there is a substantial length dependence of the $\kappa(\omega)$ spectra of the in-plane TA modes, indicating notable ballistic thermal transport characteristics. The peak value of $\kappa(\omega)$ for the 2L-SNM is $\sim 100\%$ higher than that of the 1L-SNM counterpart, indicating strong ballisticity of in-plane TA modes in these periodic, large-hole SNMs.

Figure 4(g) exhibits the spectra of $\kappa(\omega)$ for in-plane transverse modes in **ap-xy** SNMs. Comparing it with Fig. 4(c) for their periodic counterparts, it is evident that $\kappa(\omega)$ undergoes significant suppression due to aperiodicity in holes, which is notably stronger than the case for LA modes presented in Figs. 4(b) and 4(f). Moreover, $\kappa(\omega)$ for the y polarization does not exhibit significant changes with device length, indicating a more diffusive thermal transport behavior, as shown in Fig. 4(g).

3. z polarization

As depicted in Figs. 4(d) and 4(h), the z -polarization modes, which roughly represent TA and TO phonon modes polarized cross-plane (i.e., in the direction parallel to the axial direction of nanoholes), exhibit minimal involvement in thermal transport compared with longitudinal modes and in-plane transverse modes. This is evidenced by their considerably lower values of $\kappa(\omega)$ when compared with those of x and y polarizations presented in Figs. 4(b) and 4(c). Furthermore, certain z -polarization modes even display negative contributions to thermal transport within specific frequency ranges. The negative $\kappa(\omega)$ remains elusive, though we hypothesize two potential mechanisms. First, as illustrated in Figs. S7(d)–S7(f) (temperature contours) in the Supplemental Material [40], the temperature in the neck regions may exceed that in the channels at the same x coordinates, generating a temperature gradient contrary to the overall temperature gradient across the device. This phenomenon is predominantly observed in complex structures like SNMs, particularly in **ap-xy** configurations, which often display intricate spatial temperature distributions. Secondly, the negative $\kappa(\omega)$ could stem from the backscattering of phonons by holes.

Like the y -polarization transverse modes, noticeable regions with zero transmission are also observed, aligning with the band gap of transverse modes, as indicated by the dispersion relations of silicon in Fig. S1(a) in the Supplemental Material [40].

To summarize, the decomposed thermal conductivity spectra presented in Fig. 4 reveal a major contribution of LA, LO, and in-plane TA phonon modes to heat conduction in large-hole SNMs, while cross-plane transverse modes contribute negligibly to thermal transport. The **ap-x** hole distribution

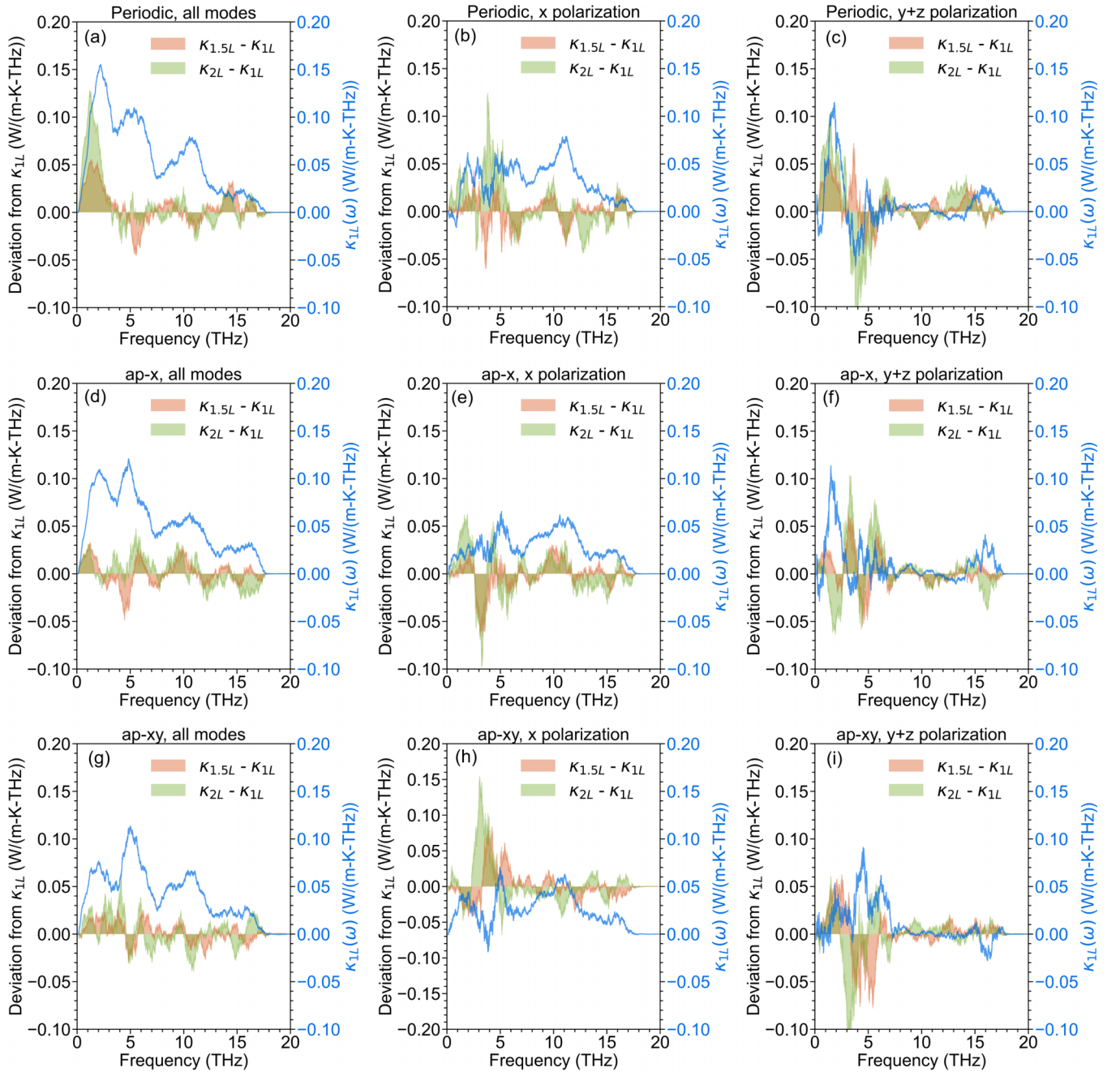


FIG. 5. Left axis (shaded area): Length-dependent deviation from spectral κ of small-hole silicon nanomeshes (SNMs) with length of $1L$ (κ_{1L} , where the subscript L denotes a device length of $L = 65$ nm); right axis (blue curve): spectral κ of κ_{1L} . (a), (d), and (g) Contributions of spectral κ from all modes for periodic, **ap-x**, and **ap-xy** SNMs, respectively. (b), (e), and (h) Contributions from x polarization. (c), (f), and (i) Contributions from the summation of y and z polarizations.

barely affects $\kappa(\omega)$, while the **ap-xy** hole distribution primarily suppresses the in-plane TA modes, while mildly suppressing the transport of LA modes.

D. Small-hole SNMs: Effect of device length on spectral phonon transport

Figure 5 presents the thermal conductivity spectra $\kappa(\omega)$ of small-hole SNMs with varying lengths and hole arrangements. In Fig. 5(a), it is evident that $\kappa(\omega)$ exhibits

significant changes with the length of periodic small-hole SNMs. Moreover, the contribution of low-frequency modes (ranging between 0 and 3 THz) to κ increases substantially in longer SNMs. This phenomenon suggests that these phonons possess long mean-free paths and consequently propagate in a rather ballistic manner within the small-hole SNM structure. These low-frequency modes, as revealed by the SED contour in Fig. 3(d), correspond to acoustic (~ 0 – 0.9 THz) and optical (~ 0.9 – 3 THz) modes belonging to the small-hole SNM lattice. These SNM modes represent coherent phonon

modes that adhere to the phonon dispersion relations of the small-hole SNM lattice [Fig. 3(d)]. Accordingly, these modes perceive the small holes as integral components constituting the unit cell of the SNM, rather than as scatterers. This is like the scenario of 1D SLs, where coherent modes do not experience any scattering at SL interfaces [48,50,53]. Furthermore, Fig. 5(d) provides additional evidence of the coherent nature of these 0–3 THz modes, where $\kappa(\omega)$ of small-hole SNMs is significantly suppressed by the aperiodicity of holes in the x direction (**ap-x**). This resembles the phenomenon of suppressed coherent phonon transport observed experimentally and in numerical modeling studies of aperiodic SLs [4,36]. Here, we emphasize that, in the particle treatment of phonons, it is expected that κ is lower in SNMs with smaller holes, particularly the κ contributed by low-frequency phonons, due to increased phonon-hole boundary scattering. While this mechanism can significantly reduce κ in the **ap-xy** structure, where the holes can directly block (and thus scatter) phonons transporting through the channels, it is not expected to cause a significant difference in the κ of periodic SNM and **ap-x** SNM. This is because both structures feature straight and unblocked channels. The reduced κ of **ap-x** observed in this paper is primarily due to the broken periodicity of the structure, which disrupts phonon coherence, as discussed in Sec. III B.

Figures 5(b) and 5(c) depict the decomposed $\kappa(\omega)$ spectra of periodic small-hole SNMs in the x and $y + z$ polarizations. We also present the spectra in y and z polarizations separately in Fig. S3 in the Supplemental Material [40]. Like the large-hole scenario [Figs. 4(b) and 4(c)], both x and y polarizations make substantial contributions to κ , with the y -polarization $\kappa(\omega)$ exhibiting a distinct cutoff at ~ 7 THz, approximately matching with the cutoff frequency of the TA phonon branch in pristine silicon (Fig. S1 in the Supplemental Material [40]). While the z -polarization phonons in small-hole SNM display a marked contribution to κ (see Fig. S6 in the Supplemental Material [40]), the z -polarization $\kappa(\omega)$ is negligible in the large-hole SNM case in Fig. 4(d).

Another notable observation in Figs. 5(b) and 5(c) is that neither the x - nor $y + z$ -polarization $\kappa(\omega)$ of small-hole SNMs exhibits a monotonic increase with SNM length. Particularly, as illustrated in Fig. 5(c), the $y + z$ -polarization $\kappa(\omega)$ in the 3.1–6.0 THz range decreases significantly when the SNM length increases from L to $2L$ (as indicated by the green shaded area). However, this does not imply a reduction in κ , as the x -polarization $\kappa(\omega)$ in the same frequency range increases by nearly the same amount. Consequently, the net change in the total κ contributed by 3.1–6.0 THz phonons is nearly zero, as demonstrated in Fig. 5(a). The nearly opposite contribution to thermal transport by x -polarization modes (roughly LO modes) and $y + z$ -polarization modes (roughly TO modes) likely arises from phonon mode conversion induced by scattering at hole boundaries, a phenomenon observed in nanoparticle-in-matrix type nanocomposites [54] and graphene-carbon nanotube networks [55].

Figure 5(d) depicts the $\kappa(\omega)$ of **ap-x** small-hole SNMs. In contrast with the large-hole cases (see Fig. S2 in the Supplemental Material [40]), the $\kappa(\omega)$ spectra of **ap-x** small-hole SNMs are notably suppressed compared with those of periodic small-hole SNMs. Specifically, the low-frequency

region from 0 to 3.4 THz exhibits the most significant reduction in $\kappa(\omega)$, which is attributed to the suppression of coherent modes in the **ap-x** structure. This observation agrees with the diminished coherent phonons observed in aperiodic SLs, where aperiodicity in the x direction disrupts the secondary periodicity of the SL, preventing the formation of long-range coherent phonons across the structure [4]. It is well understood that this effect can substantially reduce the κ of SLs. Due to the suppressed contribution of coherent phonons, the thermal conductivity spectra of **ap-x** small-hole SNMs exhibit much weaker dependence on SNM length, unlike the case of large-hole SNMs. In other words, phonons do not demonstrate notable ballistic transport behaviors in **ap-x** small-hole SNMs.

Figure 5(g) displays the $\kappa(\omega)$ of the **ap-xy** SNM. Compared with the periodic case [Fig. 5(a)] and the **ap-x** case [Fig. 5(d)], a substantial suppression in $\kappa(\omega)$ is observed in the low-frequency region (up to 3.4 THz), while high-frequency phonons remain relatively unaffected, a phenomenon readily apparent in Fig. 3(b) as well. This observation aligns with the diffusive nature of high-frequency phonons, whose transport is primarily influenced by anharmonic scatterings rather than hole boundaries.

E. Deviation from macroscopic heat conduction: Heat flux splitting

Figure 6 illustrates the x -direction heat flux (J_x), representing the overall heat flow direction in large- and small-hole SNMs with periodic, **ap-x**, and **ap-xy** hole distributions. We also present the corresponding temperature distributions for each case in Fig. S7 in the Supplemental Material [40], which show an overall monotonic decrease in the x direction.

In Fig. 6(a), J_x exhibits a continuous and relatively constant value within the channels of the periodic SNM, while it approaches zero in the neck regions. In contrast, in Fig. 6(b), for the **ap-x** SNM, J_x noticeably decreases at locations where the channel intersects with wider (in the x direction)-than-average necks. This phenomenon is prominently stronger in **ap-xy** SNMs, as shown in Fig. 6(c). Specifically, in **ap-xy** SNMs, where the channels are occasionally partially or fully obstructed, we observe large variability in the values of J_x along the heat transfer path within the channels, indicating a significant diversion of heat flow to the neck region.

Figures 6(d)–6(f) show the heat flux J_x distribution for periodic, **ap-x**, and **ap-xy** small-hole SNMs, of which the hole size is $1.5 \times 1.5 \text{ nm}^2$. Evidently, J_x is overall uniform in the channels of the periodic and **ap-x** structure, while it varies more significantly in the channels of the **ap-xy** counterpart.

The noticeable decrease in J_x at the intersections of the channel and neck indicates heat flow splitting [56], where a portion of x -direction heat current diverts into the neck region. This phenomenon is evaluated in Fig. 7 through the splitting factor, denoted as

$$\delta_{\text{splitting}} = \frac{\sum |J_y|}{\sum |J_x| + \sum |J_y|}, \quad (12)$$

where J_x and J_y denote the value of heat flux in the x (parallel to the channel) and y (perpendicular to the channel)

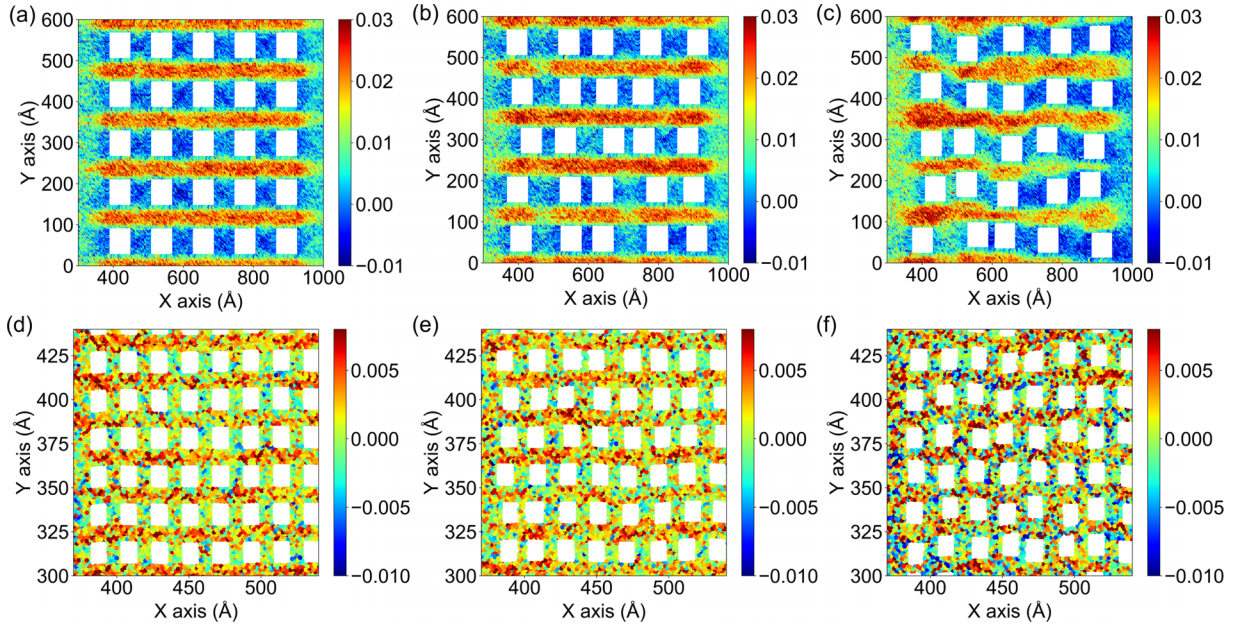


FIG. 6. x -direction heat flux J_x of both large- and small-hole silicon nanomeshes (SNMs) obtained from nonequilibrium molecular dynamics (NEMD) simulations. (a)–(c) J_x contours of periodic, **ap-x**, and **ap-xy** large-hole SNMs. (d)–(f) Zoom-in J_x contours of periodic, **ap-x**, and **ap-xy** small-hole SNMs.

directions, respectively. Heat flux splitting can occur via different mechanisms. In complex, porous structures like SNMs, this can happen due to the largely inhomogeneous temperature distribution within the structure. As shown in Fig. S7 in the Supplemental Material [40], the temperature in the neck regions can be higher than in the channel region at an upstream location, creating a slightly negative local temperature gradient. Additionally, heat flux splitting can occur when phonons are scattered at the hole boundaries, especially near the corners, diverting some phonons into the neck region.

A higher $\delta_{\text{splitting}}$ value indicates a greater diversion of heat flow into the y direction (toward the neck region), typically resulting in a reduction in κ . Interestingly, $\delta_{\text{splitting}}$ demonstrates a notable increase with the level of aperiodicity in large-hole SNMs, while it displays less dependence on aperiodicity in small-hole SNMs. These findings contrast with the trends observed in the κ data presented in Fig. 2, which

show a significant reduction in κ due to partial (**ap-x**) or full aperiodicity (**ap-xy**) in hole locations in small-hole SNMs. Consequently, we argue that, while heat splitting offers insights into heat transfer from a macroscopic perspective, it may not fully elucidate nanoscale thermal transport behaviors in NMs containing small holes, although it might provide reasonably accurate guidance for SNMs with larger holes, exceeding tens of nanometers or even micron-sized ones.

Lastly, it is noteworthy that small-hole SNMs exhibit higher $\delta_{\text{splitting}}$ values compared with large-hole SNMs, which contributes significantly to the notable difference in κ between the two. However, the principal reason for this contrast remains rooted in the fact that the greater abundance of nanoholes in small-hole SNMs induces a more extensive scattering of phonons, like in the case of the nanoparticle-in-matrix type of nanocomposite [50].

F. Deviation from macroscopic heat conduction: Shape factor

Shape factor (S) is frequently employed in macroscopic heat transfer analyses as a straightforward method for estimating heat flow in heat conduction scenarios. For instance, the shape factor of a slab containing arrays of holes can be computed as [31,57]

$$S = \frac{1}{\int \frac{dx}{A(x)}} = \frac{q_x}{\kappa_x \Delta T}, \quad (13)$$

where $A(x)$ is the cross-sectional area of the structure perpendicular to x direction, q_x is steady-state heat current, and ΔT is the temperature difference between the two ends. Mathematically, a NM with hole positions more widely dispersed along the x direction will yield a higher S , consequently leading to a higher effective κ . Wei *et al.* [31] conducted regression analysis demonstrating the efficacy of S in categorizing the κ

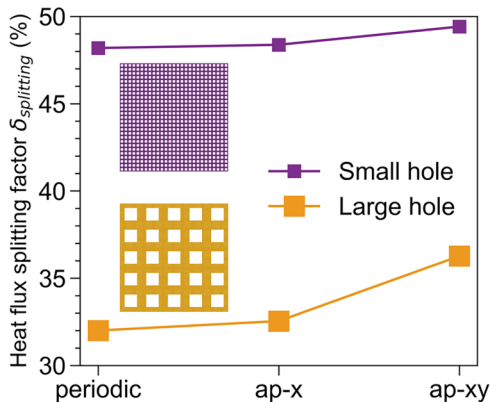


FIG. 7. Heat flux splitting factor $\delta_{\text{splitting}}$ in large- and small-hole silicon nanomeshes (SNMs).

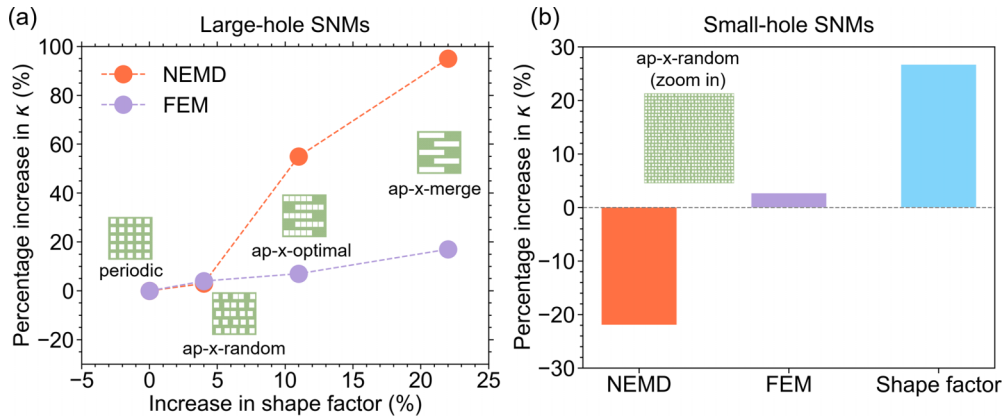


FIG. 8. (a) Large-hole silicon nanomeshes (SNMs): The percentage increase in κ of three types of **ap-x** structures compared with the κ of their periodic counterparts is plotted against the corresponding increase in shape factor. These results show an overall good quantitative agreement between S and finite element method (FEM) results, but only qualitative agreement between S and nonequilibrium molecular dynamics (NEMD) results. This discrepancy indicates significant nondiffusive heat conduction in NEMD simulations. (b) Small-hole SNMs: NEMD predicts a reduced κ , while the shape factor suggests an increase in κ . This discrepancy indicates the inapplicability of the shape factor in describing thermal transport in small-hole SNMs due to prominent nondiffusive and wave effects.

of GNMs, displaying reasonable agreement with predictions by BTE simulations.

In this paper, we explore the applicability of S for both large- and small-hole SNMs, recognizing that S originated from classical, diffusive heat transfer theories. To achieve this, we examine three distinctive hole distributions within the SNM: (1) **ap-x-random**, characterized by randomly generated hole distributions without any imposed constraints; (2) **ap-x-optimal**, as identified in this paper through shape-factor analysis and further tested to possess even higher κ than the structure optimized in Ref. [31] to have the highest κ among NM configurations; (3) **ap-x-merge**, resembling **ap-x-optimal** but with all holes in each column consolidated into a single large rectangular hole along the heat flow direction.

Two approaches are used to evaluate κ of these structures: NEMD simulations as used in previous sections of this paper, which capture the actual coherent or incoherent phonon transport and scattering behaviors, and finite element method (FEM) simulations based on Fourier's law of heat conduction. The SNM structures simulated in FEM share geometric similarities (in aspect ratio and hole locations) with those used in NEMD but are 10^6 times larger. Thus, the FEM results represent macroscopic heat conduction scenarios. For the FEM simulations, we used the thermal properties of silicon: a κ of 140 W/m K, a density of 2,330 kg/m³, and a specific heat of 710 J/kg K. The element size for the large-hole SNM was 0.5 mm (hole size is 7.2×7.2 mm), while a smaller mesh size of 0.1 mm was used for the small-hole cases (hole size is 1.5×1.5 mm). Like our NEMD simulations, a hot bath at 330 K and a cold bath at 270 K were used to induce heat current across the SNM device. The κ of the SNM was computed using Fourier's law as $\kappa = qL/(A_c\Delta T)$, where q is the heat current obtained from the FEM simulation.

Figure 8(a) illustrates the increase in κ as predicted by NEMD and FEM simulations with respect to the corresponding shape factor S . Specifically, the x axis denotes the increase in shape factor for the three random structures (**ap-x-random**, **ap-x-optimal**, and **ap-x-merge**) with

respect to the shape factor of their periodic counterpart. The y axis shows the increase in κ as predicted by NEMD and FEM simulations. The percentage increase is calculated as $[(\kappa_{\text{ap-x}}/\kappa_{\text{periodic}}) - 1] \times 100\%$: for the NEMD data series, it is computed using the κ values predicted by NEMD, while for the FEM data series, the κ values predicted from FEM are used.

As depicted in Fig. 8(a), the FEM simulation consistently predicts higher κ for SNM structures with larger shape factors, reaffirming the utility of S in broadly classifying the relative κ of macroscopic structures. However, the κ values predicted by S , exhibit disproportionately large variations with S . Notably, the κ of the **ap-x-merge** structure is $\sim 95\%$ higher than that of its periodic counterpart, despite its shape factor S being only 22% higher. This disparity is even larger in small-hole SNMs, as elaborated below.

Illustrated in Fig. 8(b) is the analysis of an **ap-x** small-hole SNM structure. The shape factor S of this structure surpasses that of its periodic counterpart by 27%, while FEM predicts a mere 3% increase in κ . Moreover, NEMD predicts a reduction of $>22\%$ in the κ of this **ap-x** structure compared with its periodic counterpart. This discrepancy underscores the inadequacy of both S and FEM, or any macroscopic heat conduction laws, as dependable tools for categorizing the κ of small-hole SNMs, where considerations such as ballistic phonon transport and the wave nature of phonons become pivotal.

IV. CONCLUSIONS

In this paper, we systematically investigated the spectral thermal transport properties of SNMs featuring both large and small holes, arranged periodically, aperiodically in the x direction (**ap-x**), which maintains the original straight channels of periodic SNMs, and fully aperiodically (**ap-xy**). Our combined NEMD and EMD simulations consistently revealed a notable reduction in the κ of small-hole SNMs due to the **ap-x** structure, a phenomenon not observed in large-hole

SNMs. Through spectral thermal conductivity analysis, we unveiled that **ap-x** aperiodicity in hole locations markedly dampens low-frequency phonons in small-hole SNMs, resembling the behavior seen in 1D SLs where interface aperiodicity effectively hinders coherent phonon transport. Direct confirmation of coherent phonon modes (or SNM modes) in the 0–3 THz frequency range was achieved via SED analysis. Furthermore, our investigations into SNMs of varying lengths demonstrated the ballistic propagation of these low-frequency phonons within small-hole SNMs, highlighting their coherent nature. Conversely, the impact of **ap-x** hole distribution on the κ of large-hole SNMs was found to be negligible, mainly due to the prevention of coherent phonon formation when large holes exceed the spatial coherence length of phonons.

Additionally, in this paper, we show that, regardless of their size, holes can significantly reduce the κ of phonons across all frequencies, with higher-frequency phonons typically experiencing stronger scattering by holes. Moreover, for SNMs with equivalent overall porosity, smaller holes exhibit a more pronounced scattering effect on phonons, resulting in lower κ values for small-hole SNMs compared with large-hole counterparts. Remarkably, our findings reveal that, in small-hole SNMs, low-frequency phonons (in the 0–3 THz range) can even exhibit higher heat transfer capabilities than those in large-hole SNMs within the same frequency range. This observation underscores the unique characteristics of coherent modes, which can traverse the SNM structure without encountering scattering by the holes, akin to coherent phonons in SLs that remain unscattered at interfaces.

Lastly, we examined the effectiveness of heat flux splitting factor and shape factor, two parameters derived from macroscopic descriptions of heat conduction, in categorizing the relative κ values of SNMs with different hole distributions. Our analysis concluded that, while both factors perform adequately for large-hole SNMs (where the feature size exceeds the spatial coherence length of phonons), their utility for small-hole SNMs may be unreliable, whether for qualitative or quantitative analyses. In summary, the analysis and prediction of thermal transport in small-hole SNMs should consider coherent phonon behaviors, particularly when the hole feature size is comparable with or smaller than the spatial coherence length of phonons, highlighting the pivotal role of wave nature in such scenarios.

ACKNOWLEDGMENTS

H.C., T.M., and Y.W. acknowledge the support provided by the Division of Chemical, Bioengineering, Environmental, and Transport Systems of the National Science Foundation of the United States (Award No. 2047109). T.M. and Y.W. acknowledge the support provided by the Division of Civil, Mechanical, and Manufacturing Innovation of the National Science Foundation of the United States (Award No. 1826392). Additionally, the authors wish to acknowledge the assistance provided by the Research and Innovation, and Cyberinfrastructure Team within the Office of Information Technology at the University of Nevada, Reno, for their facilitation and access to the Pronghorn High-Performance Computing Cluster.

-
- [1] M. V. Simkin and G. D. Mahan, Minimum thermal conductivity of superlattices, *Phys. Rev. Lett.* **84**, 927 (2000).
 - [2] B. Yang and G. Chen, Partially coherent phonon heat conduction in superlattices, *Phys. Rev. B* **67**, 195311 (2003).
 - [3] M. N. Luckyanova, J. Garg, K. Esfarjani, A. Jandl, M. T. Bulsara, A. J. Schmidt, A. J. Minnich, S. Chen, M. S. Dresselhaus, Z. Ren *et al.*, Coherent phonon heat conduction in superlattices, *Science* **338**, 936 (2012).
 - [4] Y. Wang, H. Huang, and X. Ruan, Decomposition of coherent and incoherent phonon conduction in superlattices and random multilayers, *Phys. Rev. B* **90**, 165406 (2014).
 - [5] Y. Wang, C. Gu, and X. Ruan, Optimization of the random multilayer structure to break the random-alloy limit of thermal conductivity, *Appl. Phys. Lett.* **106**, 073104 (2015).
 - [6] G. Xie, D. Ding, and G. Zhang, Phonon coherence and its effect on thermal conductivity of nanostructures, *Adv. Phys.: X* **3**, 1480417 (2018).
 - [7] Z. Zhang, Y. Guo, M. Bescond, J. Chen, M. Nomura, and S. Volz, Coherent thermal transport in nano-phononic crystals: An overview, *APL Mater.* **9**, 081102 (2021).
 - [8] R. Anufriev, J. Maire, and M. Nomura, Review of coherent phonon and heat transport control in one-dimensional phononic crystals at nanoscale, *APL Mater.* **9**, 070701 (2021).
 - [9] E. S. Landry, M. I. Hussein, and A. J. H. McGaughey, Complex superlattice unit cell designs for reduced thermal conductivity, *Phys. Rev. B* **77**, 184302 (2008).
 - [10] P. Chakraborty, I. A. Chiu, T. Ma, and Y. Wang, Complex temperature dependence of coherent and incoherent lattice thermal transport in superlattices, *Nanotechnology* **32**, 065401 (2021).
 - [11] J.-K. Yu, S. Mitrovic, D. Tham, J. Varghese, and J. R. Heath, Reduction of thermal conductivity in phononic nanomesh structures, *Nat. Nanotechnol.* **5**, 718 (2010).
 - [12] N. Zen, T. A. Puurtinen, T. J. Isotalo, S. Chaudhuri, and I. J. Maasilta, Engineering thermal conductance using a two-dimensional phononic crystal, *Nat. Commun.* **5**, 3435 (2014).
 - [13] S. Alaie, D. F. Goettler, M. Su, Z. C. Leseman, C. M. Reinke, and I. El-Kady, Thermal transport in phononic crystals and the observation of coherent phonon scattering at room temperature, *Nat. Commun.* **6**, 7228 (2015).
 - [14] M. R. Wagner, B. Graczykowski, J. S. Reparaz, A. El Sachat, M. Sledzinska, F. Alzina, and C. M. Sotomayor Torres, Two-dimensional phononic crystals: Disorder matters, *Nano Lett.* **16**, 5661 (2016).
 - [15] J. Lee, W. Lee, G. Wehmeyer, S. Dhuey, D. L. Olynick, S. Cabrini, C. Dames, J. J. Urban, and P. Yang, Investigation of phonon coherence and backscattering using silicon nanomeshes, *Nat. Commun.* **8**, 14054 (2017).
 - [16] Z. Xiong, X. Wang, K. H. K. Lee, X. Zhan, Y. Chen, and J. Tang, Thermal transport in supported graphene nanomesh, *ACS Appl. Mater. Interfaces* **10**, 9211 (2018).
 - [17] P. Schelling and S. Phillpot, Multiscale simulation of phonon transport in superlattices, *J. Appl. Phys.* **93**, 5377 (2003).

- [18] T. Ma and Y. Wang, *Ex-situ* modification of lattice thermal transport through coherent and incoherent heat baths, *Mater. Today Phys.* **29**, 100884 (2022).
- [19] T. Ma, C.-T. Lin, and Y. Wang, The dimensionality effect on phonon localization in graphene/hexagonal boron nitride superlattices, *2D Mater.* **7**, 035029 (2020).
- [20] J. Bai, X. Zhong, S. Jiang, Y. Huang, and X. Duan, Graphene nanomesh, *Nat. Nanotechnol.* **5**, 190 (2010).
- [21] D. Wang, Y. Dou, X. Zhang, K. Bi, I. R. Panneerselvam, H. Sun, X. Jiang, R. Dai, K. Song, H. Zhuang *et al.*, Manufacturing and applications of multi-functional holey two-dimensional nanomaterials a review, *Nano Today* **55**, 102162 (2024).
- [22] J. N. Kirchof, K. Weinel, S. Heeg, V. Deinhart, S. Kovalchuk, K. Höflich, and K. I. Bolotin, Tunable graphene phononic crystal, *Nano Lett.* **21**, 2174 (2021).
- [23] L. Cui, G. Wei, Z. Li, and X. Du, Thermal transport in graphene nanomesh: Unraveling the role of Brillouin zone folding, phonon localization and phonon confinement, *Int. J. Heat Mass Transf.* **165**, 120685 (2021).
- [24] P. E. Hopkins, C. M. Reinke, M. F. Su, R. H. I. Olsson, E. A. Shaner, Z. C. Leseman, J. R. Serrano, L. M. Phinney, and I. El-Kady, Reduction in the thermal conductivity of single crystalline silicon by phononic crystal patterning, *Nano Lett.* **11**, 107 (2011).
- [25] Y. Liao, T. Shiga, M. Kashiwagi, and J. Shiomi, Akhiezer mechanism limits coherent heat conduction in phononic crystals, *Phys. Rev. B* **98**, 134307 (2018).
- [26] H. Cui, T. Ma, and Y. Wang, Elucidating optimal nanohole structures for suppressing phonon transport in nanomeshes, *2D Mater.* **11**, 035026 (2024).
- [27] J. Maire, R. Anufriev, R. Yanagisawa, A. Ramiere, S. Volz, and M. Nomura, Heat conduction tuning by wave nature of phonons, *Sci. Adv.* **3**, e1700027 (2017).
- [28] L. Hu and D. Maroudas, Thermal transport properties of graphene nanomeshes, *J. Appl. Phys.* **116**, 184304 (2014).
- [29] T. Feng and X. Ruan, Ultra-low thermal conductivity in graphene nanomesh, *Carbon* **101**, 107 (2016).
- [30] S. Hu, Z. Zhang, P. Jiang, J. Chen, S. Volz, M. Nomura, and B. Li, Randomness-induced phonon localization in graphene heat conduction, *J. Phys. Chem. Lett.* **9**, 3959 (2018).
- [31] H. Wei, H. Bao, and X. Ruan, Genetic algorithm-driven discovery of unexpected thermal conductivity enhancement by disorder, *Nano Energy* **71**, 104619 (2020).
- [32] H. Wei, Y. Hu, H. Bao, and X. Ruan, Quantifying the diverse wave effects in thermal transport of nanoporous graphene, *Carbon* **197**, 18 (2022).
- [33] P. Chakraborty, L. Cao, and Y. Wang, Ultralow lattice thermal conductivity of the random multilayer structure with lattice imperfections, *Sci. Rep.* **7**, 8134 (2017).
- [34] M. N. Luckyanova, J. Mendoza, H. Lu, B. Song, S. Huang, J. Zhou, M. Li, Y. Dong, H. Zhou, J. Garlow *et al.*, Phonon localization in heat conduction, *Sci. Adv.* **4**, eaat9460 (2018).
- [35] R. Hu, S. Iwamoto, L. Feng, S. Ju, S. Hu, M. Ohnishi, N. Nagai, K. Hirakawa, and J. Shiomi, Machine-learning-optimized aperiodic superlattice minimizes coherent phonon heat conduction, *Phys. Rev. X* **10**, 021050 (2020).
- [36] P. Chakraborty, Y. Liu, T. Ma, X. Guo, L. Cao, R. Hu, and Y. Wang, Quenching thermal transport in aperiodic superlattices: A molecular dynamics and machine learning study, *ACS Appl. Mater. Interfaces* **12**, 8795 (2020).
- [37] A. P. Thompson, H. M. Aktulga, R. Berger, D. S. Bolintineanu, W. M. Brown, P. S. Crozier, P. J. in't Veld, A. Kohlmeyer, S. G. Moore, T. D. Nguyen *et al.*, LAMMPS—A flexible simulation tool for particle-based materials modeling at the atomic, meso, and continuum scales, *Comput. Phys. Commun.* **271**, 108171 (2022).
- [38] F. H. Stillinger and T. A. Weber, Computer simulation of local order in condensed phases of silicon, *Phys. Rev. B* **31**, 5262 (1985).
- [39] M. Kaviany, *Heat Transfer Physics* (Cambridge University Press, Cambridge, 2008).
- [40] See Supplemental Material at <http://link.aps.org/supplemental/10.1103/PhysRevB.110.075301> for additional data on phonon properties and thermal conductivities of silicon nanomeshes.
- [41] Y. Liu, R. Hu, Y. Wang, J. Ma, Z. Yang, and X. Luo, Big-data-accelerated aperiodic Si/Ge superlattice prediction for quenching thermal conduction via pattern analysis, *Energy AI* **3**, 100046 (2021).
- [42] K. Säskilähti, J. Oksanen, J. Tulkki, and S. Volz, Role of anharmonic phonon scattering in the spectrally decomposed thermal conductance at planar interfaces, *Phys. Rev. B* **90**, 134312 (2014).
- [43] K. Säskilähti, J. Oksanen, S. Volz, and J. Tulkki, Frequency-dependent phonon mean free path in carbon nanotubes from nonequilibrium molecular dynamics, *Phys. Rev. B* **91**, 115426 (2015).
- [44] J. A. Thomas, R. M. Iutzi, and A. J. H. McGaughey, Thermal conductivity and phonon transport in empty and water-filled carbon nanotubes, *Phys. Rev. B* **81**, 045413 (2010).
- [45] T. Feng, B. Qiu, and X. Ruan, Anharmonicity and necessity of phonon eigenvectors in the phonon normal mode analysis, *J. Appl. Phys.* **117**, 195102 (2015).
- [46] P. K. Schelling, S. R. Phillpot, and P. Keblinski, Comparison of atomic-level simulation methods for computing thermal conductivity, *Phys. Rev. B* **65**, 144306 (2002).
- [47] T. Maranets, M. Nasiri, and Y. Wang, Influence of spatial coherence on phonon transmission across aperiodically arranged interfaces, *Phys. Lett. A* **512**, 129572 (2024).
- [48] T. Maranets and Y. Wang, Prominent phonon transmission across aperiodic superlattice through coherent mode-conversion, *Appl. Phys. Lett.* **125**, 042205 (2024).
- [49] B. Cai, J. Pei, J. Dong, H.-L. Zhuang, J. Gu, Q. Cao, H. Hu, Z. Lin, and J.-F. Li, (Bi,Sb)₂Te₃/SiC nanocomposites with enhanced thermoelectric performance: Effect of SiC nanoparticle size and compositional modulation, *Sci. China Mater.* **64**, 2551 (2021).
- [50] T. Maranets, H. Cui, and Y. Wang, Lattice thermal conductivity of embedded nanoparticle composites: The role of particle size distribution, *Nanotechnology* **35**, 055701 (2024).
- [51] B. Baer, D. G. Walker, and L. Lindsay, Phonon transport governed by intrinsic scattering in short-period AlN/GaN superlattices, *Phys. Rev. B* **109**, 104310 (2024).
- [52] N. K. Ravichandran and A. J. Minnich, Coherent and incoherent thermal transport in nanomeshes, *Phys. Rev. B* **89**, 205432 (2014).
- [53] B. Latour and Y. Chalopin, Distinguishing between spatial coherence and temporal coherence of phonons, *Phys. Rev. B* **95**, 214310 (2017).

- [54] T. Maranets and Y. Wang, Ballistic phonon lensing by the non-planar interfaces of embedded nanoparticles, *New J. Phys.* **25**, 103038 (2023).
- [55] J. Shi, Y. Dong, T. Fisher, and X. Ruan, Thermal transport across carbon nanotube-graphene covalent and van der Waals junctions, *J. Appl. Phys.* **118**, 044302 (2015).
- [56] A. Yousefzadi Nobakht, S. Shin, K. D. Kihm, D. C. Marable, and W. Lee, Heat flow diversion in supported graphene nanomesh, *Carbon* **123**, 45 (2017).
- [57] T. L. Bergman, A. S. Lavine, F. P. Incropera, and D. P. DeWitt, *Introduction to Heat Transfer* (John Wiley & Sons, Hoboken, 2011).